Universal input-output model of GFM functions and data-driven verification methods

Dominic Groß[1], Deepak Ramasubramanian[2], and Benjamin Paz[2]

1 University of Wisconsin-Madison
2 Electric Power Research Institute

NREL Technical Monitor: Ben Kroposki

Suggested Citation

Groß, Dominic, Deepak Ramasubramanian, Benjamin Paz. December 2022. *Universal input-output model of GFM functions and data-driven verification methods*. UNIFI-2022-4-1.

DISCLAIMER

NREL is a national laboratory of the U.S. Department of Energy
Office of Energy Efficiency & Renewable Energy
Operated by the Alliance for Sustainable Energy, LLC

This report is available at no cost from the National Renewable Energy Laboratory (NREL) at www.nrel.gov/publications.

Contract No. DE-AC36-08GO28308

Technical Report
NREL/TP-5D00-88646
February 2024

National Renewable Energy Laboratory
15013 Denver West Parkway
Golden, CO 80401
303-275-3000 • www.nrel.gov

Executive Summary

An overarching goal of the UNiversal Interoperability for grid-Forming Inverters (UNIFI) Consortium is to develop vendor agnostic specifications and guidelines that ensure interoperability of gridforming (GFM) inverter-based resources (IBRs) without requiring vendors or system operators to reveal proprietary information. These UNIFI principles and specifications are envisioned to apply to a wide range of technologies and systems. The initial work on the UNIFI principles and specifications has focused on performance requirements and high-level aspirational principles outlined in [1]. Going forward, a key question is how to translate such high-level requirements and principles into rigorous specifications that can be enforced and validated for a wide range of IBRs.

A wide range of different GFM controls are available in the literature that use vastly different internal dynamics and control parameters (e.g., droop coefficients, virtual inertia constants, virtual oscillator gains). However, from a system-level viewpoint, these GFM controls implement a few universal GFM functions to various degrees of fidelity. This report summarizes work on universal GFM input-output dynamics (i.e., the dynamic response observable on the IBR terminals) through a universal reduced-order input-output model that is parameterized in generalized system-level control parameters (i.e., parameters that translate to different gains for specific GFM controls). Specifically, the input-output models presented in this work are suitable to capture the small-signal response under nominal operating conditions. After presenting the modeling approach and several examples of how standard GFM controls map to the universal input-output model, we present a first attempt to map UNIFI performance requirements for operation within normal grid conditions [1] to specifications on the input-output dynamics.

We emphasize that the main purpose of the input-output models is not to develop models for simulation but rather to obtain low-dimensional models of the IBR terminal behavior that can be used to formulate and validate vendor and technology-agnostic unit-level specifications that ensure stability, interoperability, and performance. To this end, a crucial question is how to verify if a GFM IBR conforms to the universal input-output dynamics with given generalized system-level control parameters without detailed information of the internal hardware and controls. To this end, we discuss two methods for identifying the input-output (i.e., terminal) dynamic behavior of GFM converters from input-output data that can be obtained using hardware experiments or blackbox models. The results on input-output modeling form the basis for developing stability certificates that can be directly verified through (experimental) input-output data. Moreover, we envision using the input-output modeling framework to develop and validate specifications that narrow down the class of interoperable GFM dynamics to obtain bounds on the unit-level dynamics within which vendors can innovate while interoperability and stability are ensured.

Table of Contents

List of Figures

List of Tables

1 Universal input-output models

A wide range of different GFM controls are available in the literature that use vastly different internal dynamics and control parameters (e.g., droop coefficients, virtual inertia constants, virtual oscillator gains). However, from a system-level viewpoint, these GFM controls implement a few universal GFM functions to various degrees of fidelity. We will first develop a class of common transfer function models that reveal the common features of various GFM controls and generalized control parameters that parameterize their dynamic response.

1.1 Motivation and problem setup

To better understand the common features of various GFM controls we first discuss models of GFM IBRs that arise as linearization of different GFM controls. To this end, we consider a two-bus system of an IBR connected to an infinite bus. Conceptually, a GFM IBR is often modeled as a controlled voltage source (see Figure 1a) while a GFL IBR is often modeled as a controlled current source (see Figure 1b) [1, Sec. 1.1]. For the purpose of developing input-output models we will first consider models of IBRs that fall into this standard categorization. However, we emphasize that the methods for specifying and verifying performance objectives will not be based on this assumption. Instead, the proposed methods will rely only on characterizing the static and dynamic relationship between the signals at the IBR terminal in response to perturbations of the infinite bus voltage or IBR load. Notably, this approach does not require considering specific IBR signals as IBR control inputs but instead characterizes the IBRs closed-loop response as seen from the system.

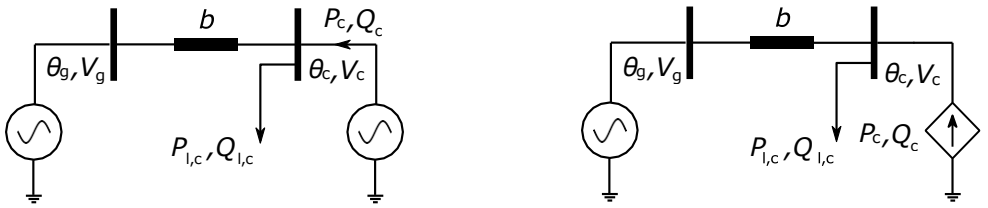

(a) GFM IBR **(b)** GFL IBR

Figure 1. Two-node system with prototypical GFM IBR modeled as controlled voltage source and prototypical GFL IBR modeled as controlled current source. We emphasize that θc and Vc denote the bus voltage phase angle and magnitude. We only use input-output signals at the IBR terminal that could be collected experimentally and do not consider internal voltages or voltage references.

Broadly speaking the response of the IBR can fully be characterized by the response of the signals at the IBR terminal, i.e., the IBR bus voltage phase angle θ_c, voltage magnitude V_c, and IBR power injection P_c and Q_c to perturbations of the infinite bus voltage phase angle

θ_g, infinite bus voltage magnitude V_g, and perturbations to the IBR bus load Pl,c and Pl,c. Such a model is well suited to capture the dynamics of the IBR as seen from the system-level, while not requiring knowledge of the IBR internals or its controls. We emphasize that, in contrast to several other characterizations of GFM capabilities, we do not rely on the existence or access to an internal voltage phasor reference.

Moreover, standard system identification methods can be used to recover such a model from data collected from detailed (blackbox) simulation models or hardware experiments. For example, under the status quo, a vendor that does not want to reveal its proprietary hardware or controls could apply the data-driven validation methods discussed in this deliverable to a detailed model (or replicate the setup from Figure 1 in a hardware experiment) and share the results of the data-driven validation method in addition to sharing a blackbox simulation model when required[1]. Future work will investigate if data-driven verification methods can be leveraged to supplement or partially replace detailed time domain-simulations.

This general line of inquiry leads to several questions that this deliverable attempts to answer. First, we attempt to map various controls proposed in the literature to input-output models to establish a baseline for the expected performance of standard GFM and GFL controls. Second, we use a few initial examples to illustrate how the UNIFI performance requirements for operation within normal grid conditions [1] can be mapped to formal and verifiable specifications on the input-output dynamics. Finally, we investigate how and to what level of accuracy the input-output dynamics can be identified using data-driven methods that only use measurement data from the setup in Figure 1 without access to internal IBR signals.

1.2 Reduced-order analytical models

We begin by modeling the network in Figure 1. Using a standard linearized quasi-static power flow model, the power injection of the IBR is modeled by

$$\begin{bmatrix} P_c \\ Q_c \end{bmatrix} = \underbrace{\begin{bmatrix} \frac{V^\star V^\star X}{R^2+X^2} & \frac{V^\star R}{R^2+X^2} \\ -\frac{V^\star V^\star R}{R^2+X^2} & \frac{V^\star X}{R^2+X^2} \end{bmatrix}}_{=:G_{\text{pf}}} \begin{bmatrix} \theta_c - \theta_g \\ V_c - V_g \end{bmatrix} + \begin{bmatrix} P_{\text{l,c}} \\ Q_{\text{l,c}} \end{bmatrix}, \tag{2.1}$$

where X and R denote the reactance and resistance of the connection to the infinite bus, and $V^\star$ denotes the nominal infinite bus and IBR voltage magnitude that is assumed to be identical. For brevity of the notation, all variables denote deviations from their nominal value in a synchronous reference frame with nominal frequency. Moreover, one may consider a dynamic model that arises from linearizing the dynamics of an inductive-resistive circuit element [2].

[1] In North America, models do not have to be provided for generation sources below 75 MVA and generation sources connected lower than transmission.

$$\begin{bmatrix} P_c \\ Q_c \end{bmatrix} = \underbrace{\frac{1}{L}\frac{1}{s^2+2\rho s+\omega_0^2+\rho^2}\begin{bmatrix} V^\star V^\star \omega_0 & V^\star(\rho+s) \\ V^\star V^\star(\rho+s) & V^\star \omega_0 \end{bmatrix}}_{=:G_{\mathbf{N}}(s)} \begin{bmatrix} \theta_c - \theta_g \\ V_c - V_g \end{bmatrix} + \begin{bmatrix} P_{\mathrm{l,c}} \\ Q_{\mathrm{l,c}} \end{bmatrix}, \tag{2.2}$$

where ρ denotes the inductance-resistance ratio ρ = R/L of the transmission line in Figure 1. For clarity of the presentation, we will focus on the model (2.1) for analytical derivations and only consider (2.2) if needed to explain the impact of network circuit dynamics. The reader is referred to [2] for a more in-depth discussion of the impact of the network circuit dynamics (2.2) on frequency stability of converter-dominated power systems.

Given the network model, we model the GFM IBR dynamics as a transfer function from the power injection Pc and Qc to the phase angle θ_c and magnitude V_c of the voltage imposed by the GFM IBR at its bus. We emphasize that this modeling assumption is not a restriction for the input-output framework to be developed but merely accounts for the fact that, to the best of the authors' knowledge, all GFM IBR controls discussed in the literature can be abstracted by this model. Specifically, we assume that

$$\begin{bmatrix} \theta_c \\ V_c \end{bmatrix} = \underbrace{\begin{bmatrix} \frac{1}{s}G_{P_c\to\omega_c}(s) & 0 \\ 0 & G_{Q_c\to V_c}(s) \end{bmatrix}}_{=:G_{\mathbf{GFM}}} \begin{bmatrix} P_c \\ Q_c \end{bmatrix}, \tag{2.3}$$

i.e., a GFM IBR imposes a dynamic relationship between its power injection and its terminal voltage. Notably, the controller (2.3) does not induce any cross coupling between active power and voltage and reactive power and frequency. This approach is typically used in networks that are predominantly inductive. Various approaches for resistive networks or inductive-resistive networks have been proposed in the literature that induce cross coupling in (2.3) to cancel out the cross coupling in the power flow model (2.1). For inductive networks, all such controls reduce to a decoupled controller of the form (2.3). For brevity of the presentation, we will consider predominantly inductive networks in this deliverable for which both the power flow and controller can typically be assumed to be decoupled. Characterizing the impact of non-negligible network resistances on the input-output models, performance specifications, and data-driven validation methods is the focus of ongoing work. To ensure that the overall problem is well posed, we require the following assumption (see [2] for further discussion).

Assumption 1. (Stable and realizable control)
(Stable and realizable control) The transfer function $G_{Pc\to\omega c}(s)$ has all its zeroes and poles in the open left half plane and relative degree greater than or equal to minus one. The transfer function $G_{Qc\to Vc}(s)$ has all its zeroes and poles in the open left half plane and relative degree greater than or equal to zero.

This model can capture the small-signal dynamics of various standard controls. The most prevalent grid-forming control is so-called droop control [3, 4]. The design of droop control typically neglects the internal dynamics of the VSC and imposes a linear power to frequency and reactive power to voltage droop characteristic

$$G_{P_c \to \omega_c}(s) = \frac{m_p}{T_p s + 1}, \quad G_{Q_c \to V_c}(s) = \frac{m_q}{T_q s + 1}, \tag{2.4}$$

where m_p and m_q denote the active and reactive power droop coefficients. Moreover, changing coordinates, virtual synchronous machine (VSM) control [5] with virtual inertia M and virtual damping D in proportion to the VSM rating is equivalent to (2.4) with, e.g., $m_p = 1/D$ and $T_p = M/D$ (see [6]). Moreover, dispatchable virtual oscillator control for inductive networks also reduces to standard droop control near the nominal operating point [7]. Finally, so-called dual-port GFM control of voltage source converters can also be modeled by (2.4), however in this case m_p and the time constant T_p are related to the physical energy storage (i.e., the DC-link capacitor) and DC source of the voltage source converters (see [2, Sec.V-A] for further details). Similar equivalences can be obtained for a wide range of GFM controls and are summarized in Figure 2. The reader is referred to [8].

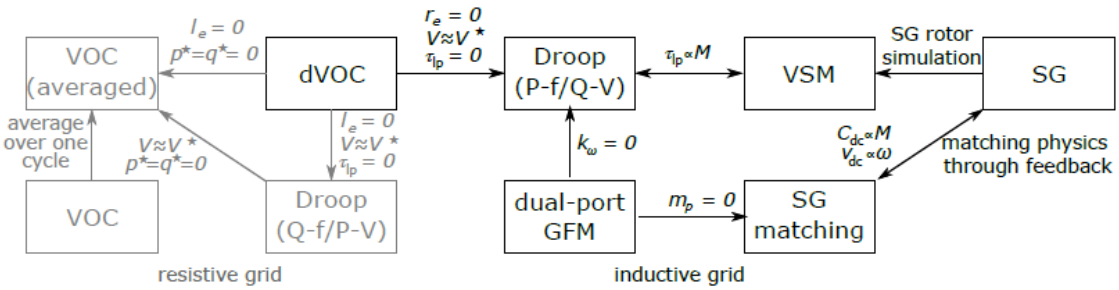

Figure 2. Conditions for equivalence of various GFM controls.

On the other hand, a GFM control without steady-state droop response is given by

$$G_{P_c \to \omega_c}(s) = \frac{\frac{k_{i,p}}{s} + k_{p,p}}{T_p s + 1}, \quad G_{Q_c \to V_c}(s) = \frac{\frac{k_{i,q}}{s} + k_q}{T_q s + 1}. \tag{2.5}$$

This control imposes a well-defined voltage (i.e., phase angle and magnitude) at the IBR terminal, but in steady state always returns to its nominal power injection and does not provide primary frequency or voltage control. This control is an example for the GFM core functionality outlined in UNIFI deliverable A3.1.1.1, that can be implemented without significant energy storage. The proportional-integral (PI) droop control (2.5) also arises when linearizing standard droop control with CERTS power limiting [9] at an operating point for which regular droop control (2.4) would result in overload of the IBR.

Overall, it can be seen that the small-signal response of various GFM IBRs can be captured through relatively simple transfer function models. A key advantage of transfer function models is that, in contrast to state space models, they result in unique minimal representations of linear time-invariant dynamics. Moreover, they can easily be visualized using, e.g., Bode and Nyquist plots.

1.3 Visualization using Bode plots and generalized GFM control parameters

By combining (2.1), (2.3), and (2.4) or (2.5), and performing standard manipulations the closed-loop transfer functions of the system shown in Figure 1 with inputs (θ_g, V_g, $P_{l,c}$,$Q_{l,c}$) and outputs (ω_c, V_c, P_c,Q_c) can be obtained and intuitively interpreted through their Bode diagram. For example, the transfer functions related to active power and frequency are shown in Table 1. It can be seen that the transfer functions are largely redundant. Thus, conceptually, all specifications could be mapped back to the GFM transfer function $G_{P_c\to\omega_c}(s)$. However, as we will see next, the interpretation and validation of the specifications is often more straightforward for the input-output pairs in Figure 1. Moreover, mapping all specifications back to the GFM transfer function $G_{P_c\to\omega_c}(s)$ may require further restrictive assumptions on the controller transfer function. Instead, we aim to impose specifications directly on the relevant input-output pairs and largely leave the control implementation open. At the same time, we will use the GFM controls (2.4) and (2.5) as examples that illustrate how the specifications can be achieved.

Table 1. Closed-loop transfer functions from external inputs to IBR terminal signals.

	ω_c	P_c
ω_g	$G_{\omega_g\to\omega_c}(s) = -\frac{1}{1+\frac{1}{b}G_{P_c\to\omega_c}(s)}$	$\frac{1}{s}G_{P_c\to\omega_c}(s)G_{\omega_g\to\omega_c}(s)$
$P_{l,c}$	$-\frac{s}{b}G_{\omega_g\to\omega_c}(s)$	$-G_{\omega_g\to\omega_c}(s)$

The Bode magnitude plot of the two transfer functions that are crucial to specify performance objective with respect to active power and frequency and typical parameters are shown in Figure 3.

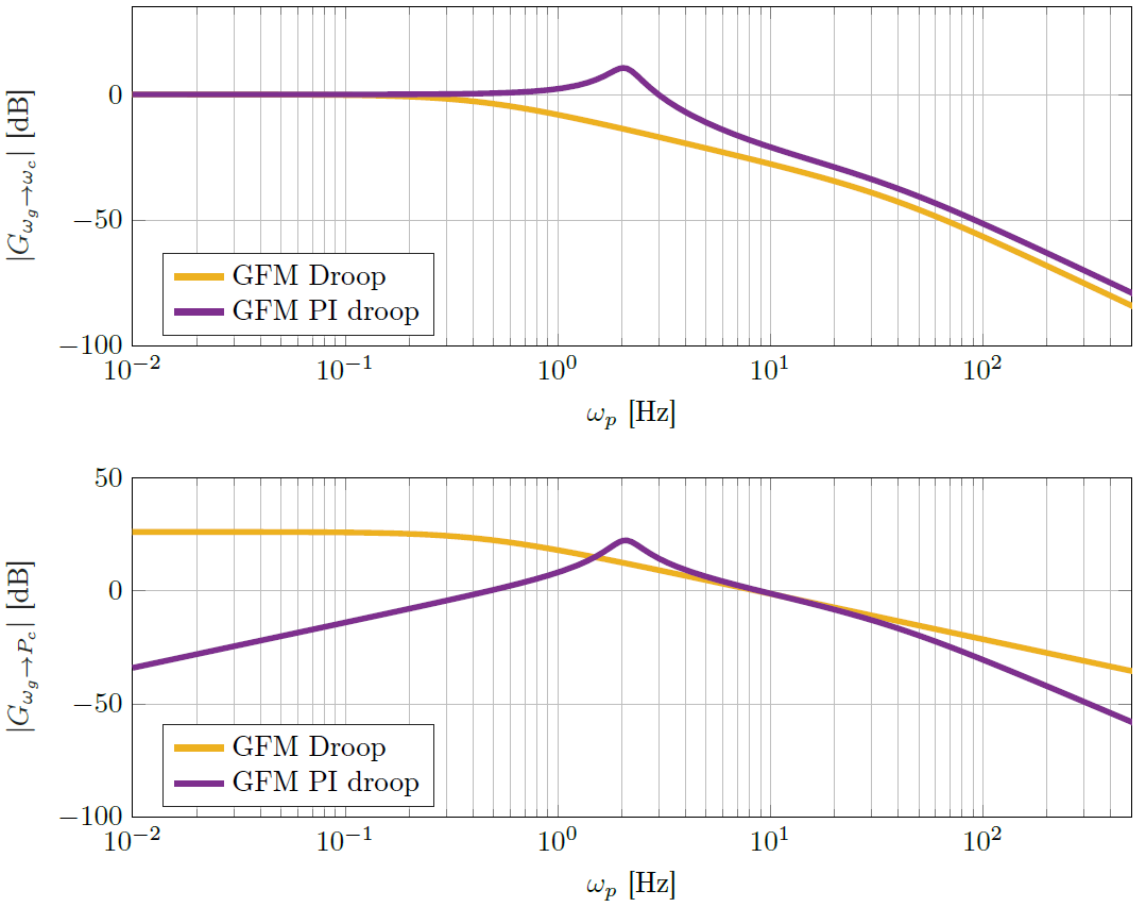

Figure 3. Bode magnitude plots of the transfer function from infinite bus frequency to IBR bus frequency and IBR active power injection.

The Bode magnitude plot models the amplitude amplification between inputs and outputs at various frequencies ω_p of the perturbation signal. In other words, if a sinusoidal perturbation of frequency ω_p is added to the input signals (e.g., ω_g) the bode plot shows the magnitude of the resulting sinusoidal response in the output (e.g., ω_c) relative to the amplitude of the input perturbation. Therefore, the Bode plots in Figure 2.3 have a straightforward interpretation. The fact that the magnitude of the transfer function $G_{\omega_g \to \omega_c}(s)$ approaches one (i.e., zero dB) for $\omega_p \to 0$ shows that the IBR bus frequency synchronizes to the infinite bus frequency in steady-state. Moreover, the fact that the plot stays close to unit gain for low perturbation frequencies implies frequency synchronization at low frequencies. However, at two hertz, the gain of GFM droop control exceeds one (i.e., zero dB) and infinite bus frequency oscillations are amplified at the IBR terminal. Beyond this perturbation frequency, the bode magnitude plot for both controls exhibits a high frequency roll off that implies that high frequency perturbations of the infinite bus frequency are suppressed at the IBR bus. It can be seen that the transfer functions and bode plots from infinite bus frequency to IBR bus frequency do not significantly differ. In fact, one

can easily re-tune the controls to achieve a perfectly matching Bode magnitude plot despite one of the two controls not providing steady-state droop. This missing information can be recovered from the second Bode magnitude plot from infinite bus frequency to IBR active power injection. The fact that the magnitude of the transfer function $G_{\omega g \rightarrow P_C}(s)$ approaches $1/m_p$ for $\omega_p \rightarrow 0$ and GFM droop control shows that the IBR injects active power in proportion to the system frequency deviation. In contrast, the $G_{\omega g \rightarrow P_C}(s)$ approaches zero for $\omega_p \rightarrow 0$ and GFM PI droop control, illustrating that GFM PI droop control does not provide a steady-state droop response. Nonetheless, both controls provide high-frequency oscillation damping.

Similar arguments can be used for the transfer functions from infinite bus voltage magnitude to IBR bus voltage magnitude and reactive power injection to interpret the main features and functions of GFM IBRs. In particular, for all the transfer functions the DC gain (i.e., for $\omega_p \rightarrow 0$) reveals the steady-state characteristics, a cut-off frequency emerges beyond which perturbations are suppressed by GFM IBRs locally, and resonances or disturbance amplifications manifest themselves as magnitude gains larger than one (i.e., zero dB).

2 Specification of GFM functions

The observations in the previous chapter enable us to formalize and validate the UNIFI performance requirements for operation within normal grid conditions [1] as further defined in Deliverable A3.1.1.1 - UNIFI Control Area Basic Terminology and Definitions.

2.1 GFM Functions

2.1.1 Droop on average frequency and average voltage

Droop on the average frequency and average voltage is commonly understood as the prototypical mechanism that governs (steady-state) transactive active and reactive power sharing. In the context of the models discussed in the previous chapter this simply translates to the specification that

$$|G_{\omega_g \rightarrow P_c}(s)| \rightarrow \frac{1}{m_p}$$

and

$$|G_{V_c \rightarrow Q_c}(s)| \rightarrow \frac{1}{m_q}$$

for $s \rightarrow 0$ and droop gains m_p and m_q. This result highlights that, similar to the droop response of synchronous generators, droop control may not necessarily be an instantaneous mechanism. However, at the same time droop on slow timescales is the basis for power-sharing and synchronization between resources. The proposed characterization clarifies that a droop is a steady-state characteristic from which IBRs or machines may deviate during transients.

2.1.2 Fast frequency response

In contrast to steady-state droop on average frequency and voltage fast frequency response seeks to provide a fast droop response with maximum response time requirements. Given a maximum response time T_{dr} and droop gain, this can be encoded in the present framework by imposing the specification that

$$|G_{\omega_g \to P_c}(j\omega_p)| \geq |\frac{m_p}{T_{dr} j\omega_p + 1}|, \forall \omega_p \geq 0, \tag{3.1}$$

in other words, that the bode magnitude plot for the IBR active power injection in response to an infinite bus frequency perturbation is above a reference plot determined by a minimum droop coefficient and response time. This constraint ensures that the IBR meets at least the minimum droop coefficient and responds at least as fast as the maximum response time.

2.1.3 Inertia & frequency smoothing

Within the context of input-output models, the equivalent function of synchronous machine inertia can be understood as the IBRs ability filter out any frequency perturbations introduced at the infinite bus, i.e., to attenuate system frequency oscillations at the IBR terminal. This capability is identical to a high-frequency roll off of the Bode magnitude plot $|G_{\omega_g \to P_c}(j\omega_p)|$. In particular, given a time constant T_ω (i.e., generalized inertia constant), this requirement can be encoded as

$$|G_{\omega_g \to \omega_c}(j\omega_p)| \leq |\frac{1}{T_\omega j\omega_p + 1}|, \forall \omega_p \geq 0, \tag{3.2}$$

in other words a larger generalized inertia constant T_ω requires the IBR to suppress frequency perturbations of lower frequency similarly to a machine with larger inertia. This requirement has also been described as frequency smoothing capability [10].

2.1.4 Passivity, damping, and interactions with other devices

Passivity and damping are specified in Deliverable A3.1.1.1 - UNIFI Control Area Basic Terminology and Definitions as the ability to

- Provide damping under all conditions, including to prevent resonances, oscillations, and instabilities, even when detailed system topology and control algorithms are unknown.
- Present passive characteristics to the grid and all its devices at all frequencies so as to prevent interactions with other grid elements.

Both of these conditions can be directly encoded using the Bode plot. In particular, the

second requirement to present passive characteristics can be encoded as an upper bound on the transfer functions from perturbation inputs to IBR terminal quantities that is less or equal than one, e.g.,

$$|G_{\omega_s \to \omega_c}(j\omega_p)| \leq 1, \forall \omega_p \geq 0, \tag{3.3}$$

This condition is sufficient to ensure that oscillations are never amplified and hence prevent resonances with other devices. Similarly, the requirement to provide damping to actively prevent resonances, oscillations, and instabilities can be encoded as a passivity constraint on the transfer function that, e.g., forces the transfer function to be positive real or meet a passivity requirement up to a multiplier [11]. These conditions can typically no longer be expressed solely on the Bode magnitude plot, but can be expressed, e.g., using a Nyquist plot obtained from magnitude and phase information (see [11] for further information).

An illustration of the various bounds on the Bode magnitude plot for GFM droop and GFM PI droop can be found in Figure 4. Moreover, Figure 4 also contains the Bode magnitude plots for a reduced-order synchronous machine (SM) and synchronous condenser (SC).

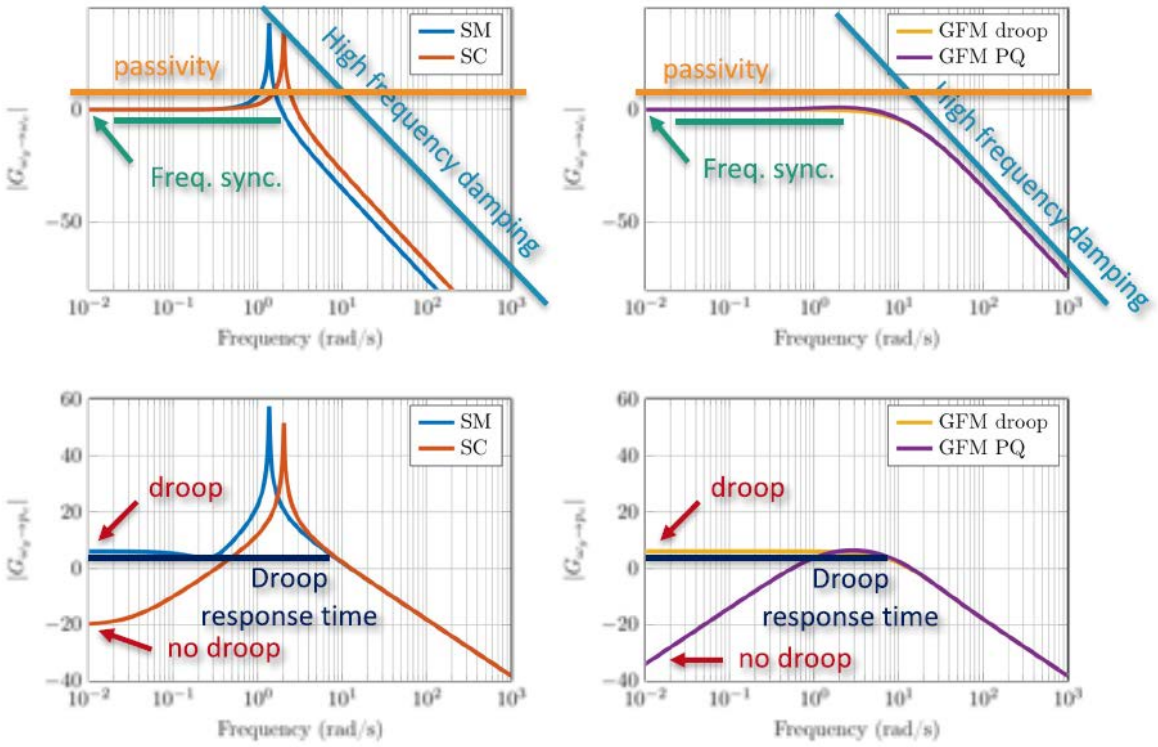

Figure 4. Bode magnitude plots of the transfer function from infinite bus frequency to IBR bus frequency and IBR active power injection as well as the corresponding transfer functions for a synchronous machine and synchronous condenser. The bounds correspond to the performance requirements discussed in this section.

2.1.5 Limitations and further specifications

The specifications so far are performance requirements during nominal and balanced operation. To formalize specifications on, e.g., power quality, the proposed framework would have to be extended to not only consider positive sequence voltage phase angles and magnitudes but voltage phase angles and magnitudes for every phase or in symmetrical components. Moreover, specifications for fault ride through and the response to large transients cannot directly be captured using the small-signal models used in this report. Nonetheless, partially encoding specifications on fault ride through is the topic of ongoing work. To this end, we first note that the proposed framework for formulating specifications does not prescribe a fixed linear time-invariant dynamic but simply prescribes bounds on the dynamics of system that are given by linear time-invariant dynamics. Moreover, the underlying dynamics may change from one operating point to the next. In other words, the proposed framework allows for nonlinear responses as long as their linearization at various operating points lies within the prescribed bounds. Moreover, a promising specification is to minimize the distance to the desired linear time-invariant dynamics (i.e., bounds) during large transients during which the IBR can no longer remain within the specified class of input-output dynamics.

2.2 Case study: GFL and GFM frequency droop control

To illustrate how the proposed framework can be used to discern different implementations of droop control and their system-level response, we consider the GFM droop control (2.4), the GFM PI droop control (2.5) and a standard grid-following implementation of droop control that relies on a Synchronous reference frame phase locked loop (SRF-PLL). The grid-following droop control is modeled using small- signal models of a phase locked loop (PLL) and corresponding filters to extract the PLL frequency.

Specifically, we model a GFL IBR as a power source (e.g., a voltage source converter with proportional- integral vector current control) that injects a controllable amount of active power. We consider a GFL IBR with frequency-watt function that uses a phase-locked loop (PLL) shown in Figure 5 to estimate the bus voltage phase angle. The power injection of the GFL IBR with frequency-watt function is given

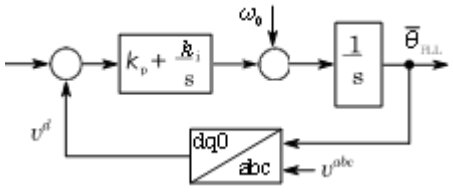

Figure 5. Phase-locked loop (PLL) used to establish a synchronous reference frame for GFL IBRs.

by $P_c = -D\omega_{PLL}$, where $D = \eta_c D_0$ and ω_{PLL} is an estimate of the frequency of the bus voltage obtained by passing the PLL angle estimate θ_{PLL} through a realizable differentiator with time constant $T_d > 0$:

$$\omega_{PLL} = \frac{s}{T_d s + 1}\theta_{PLL}. \quad (3.4)$$

To obtain the linearized reduced-order model of a GFL IBR with frequency-watt function, we solve (2.1) for θ_c, linearize the PLL dynamics shown in Figure 5, and use $P_c = -D\omega_{PLL}$ to determine the power injection of the GFL IBR. The resulting linearized reduced-order model of a GFL IBR with frequency-watt function is shown in Figure 6. We emphasize that the true frequency at the bus ω_c differs from the PLL estimate ω_{PLL} that is generated through a second-order system (i.e., the PLL) and realizable differentiator with time constant T_d. The bode magnitude plots for the three controls (i.e., GFM droop, GFL droop, and GFM PI droop) are shown in Figure 7.

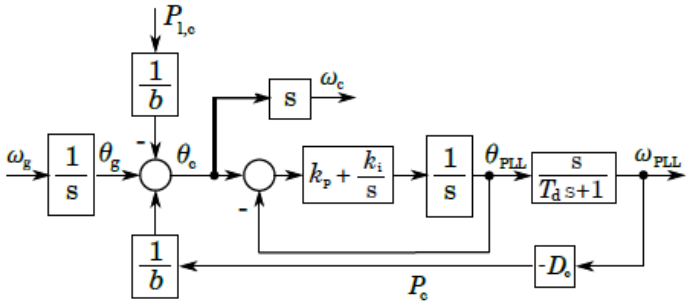

Figure 6. Linearized reduced-order model of a GFL IBR with frequency-watt function.

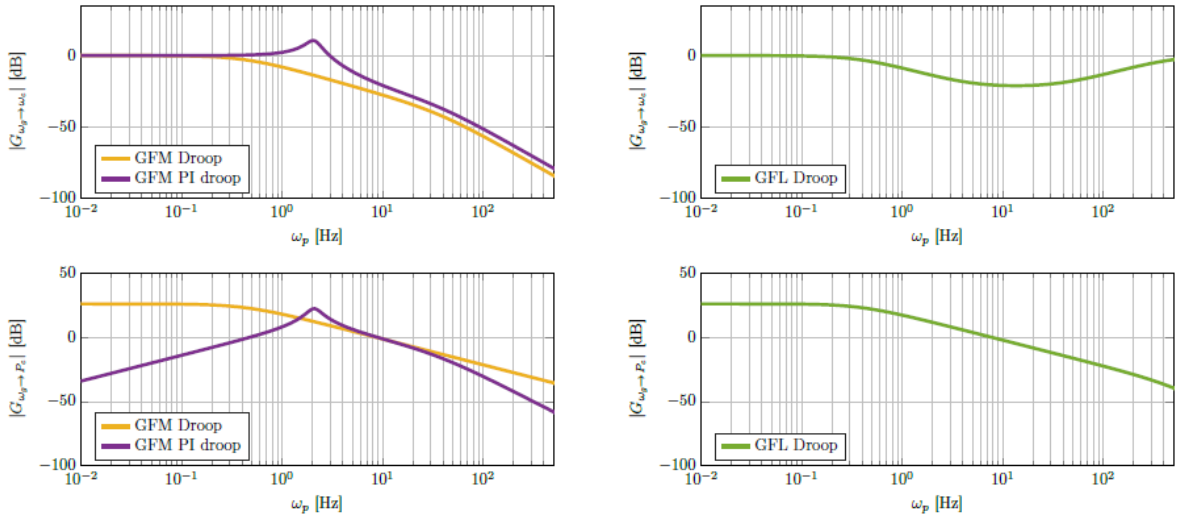

Figure 7. Bode magnitude plots for GFM droop control, GFM PI droop, and GFL droop.

It can be seen that the GFM droop control meets all the requirements outline above except for the mild resonance in $|G_{\omega g \to \omega c}(j\omega_p)|$ that does not satisfy the passivity requirement. This can be mitigated by retuning the GFM droop filter time constant and typically occurs

in GFM control if the grid coupling becomes too stiff. Otherwise, GFM droop satisfies the requirements for steady-state droop on the average frequency (with 5% droop), fast frequency response (with a cutoff frequency of 1 Hz), and an inertia-like response that attenuates frequency oscillations beyond 2 Hz at the IBR node. This corresponds to the specifications for a GFM IBR in deliverable A3.1.1.1.

Moreover, it can be seen that the GFM PI droop meets the same requirements as the GFM IBR except for the fact that it does not provide steady-state droop on the average frequency (i.e., $|G_{\omega g \rightarrow P_C}(j\omega_p)| \rightarrow 0$ as $\omega_p \rightarrow 0$). This corresponds to the specifications for GFM core IBR in deliverable A3.1.1.1.

Finally, the GFL IBR with droop meets the requirements for steady-state droop on the average frequency

$$\text{(i.e., } |G_{\omega_g \rightarrow P_c}(j\omega_p)| \rightarrow \tfrac{1}{m_p} \text{ for } \omega_p \rightarrow 0 \text{ and } m_p = 5\% \text{ p.u.)}$$

and fast frequency response (with a cutoff frequency of approximately 0.3 Hz). However, the GFL IBR does not meet the inertia and frequency smoothing requirement as $|G_{\omega g \rightarrow \omega_C}(j\omega_p)|$ does not reduce at high frequencies. In other words, perturbations to the infinite bus frequency also appear at the IBR terminal except for some attenuation in the medium frequency range. A parameter sweep and analytical computation of the cutoff frequencies of $|G_{\omega g \rightarrow \omega_C}(j\omega_p)|$ for GFL droop have been used to confirm that the inertia & frequency smoothing requirement cannot be met with a standard GFL IBR with reactive power control, active power droop based on a SRF-PLL and realizable differentiator with realistic parameters, and no explicit power oscillation damping control.

3 Data-driven verification methods

Besides the ability to formalize performance requirements in a framework with intuitive graphical interpretation, a key advantage of the input-output models considered in the previous chapter is that they are directly amenable to various data-driven methods for analysis and verification. So far, we have considered two methods. The first method uses a basic frequency sweep in the perturbation inputs to directly con- structs the Bode plots used in the previous chapter from input-output data that can be collected from a high-fidelity simulation or a hardware experiment. Moreover, standard system identification methods can be used to recover such a model from data collected from detailed (blackbox) simulation models or hardware experiments. For example, conceptually, a vendor that does not want to reveal its proprietary hardware or controls could apply either of the two data-driven validation methods discussed in this deliverable to a detailed model (or replicate the setup from Figure 1 in a hardware experiment) and share the results of the data-driven validation method to supplement blackbox simulation model when required.

3.1 Frequency sweep

Conceptually the simplest approach is to initialize a simulation model or hardware experiment that replicates the setup shown in Figure 8. Compared to the setup shown in Figure 1 used for the analytical results, a transformer has been added and detailed EMT models or actual hardware can be used. In this setting, sinusoidal perturbations are added to the system inputs (e.g., infinite bus frequency and voltage magnitude) to perturb the IBR and the response of the IBR terminal signals is recorded at various frequencies. The amplification and phase shift of the signals can be directly computed and plotted to obtain the Bode plots used in the previous chapters without access to the model or hardware internals.

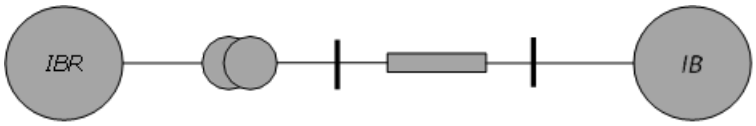

Figure 8. System model of an IBR connected to an infinite bus.

In this setup the only complication is to measure the frequency at the IBR terminal. We emphasize that the AC voltage waveform at the IBR terminal (i) does not have a well-defined frequency at all times and, (ii) that the time derivative operator is not realizable. Therefore, one can, in general not expect to compute an instantaneous frequency signal at the IBR terminal. The proposed method works around this limitation by computing the Bode magnitude plot from infinite bus angle perturbation to IBR terminal voltage phase angle perturbation by determining the magnitude of the resulting IBR terminal voltage phase angle oscillation. Specifically, at the converter AC terminal (i.e., the LCL filter capacitor) the IBR voltage phase angle relative to a rotating frame with the nominal frequency (i.e., a fictitious unperturbed infinite bus voltage phase angle). Due to the assumed linearity of the system near the nominal operating point the transfer functions from infinite bus voltage phase angle perturbation to IBR phase angle perturbation is identical to the transfer function from infinite bus frequency perturbation to IBR bus frequency.

Finally, at high perturbation frequencies additional filtering may be required to isolate the response of the GFM IBR from other modes associated with the circuit dynamics and, e.g., converter switching. If this is the case additional post-processing through, e.g., band pass filters can be used. However, we observe that the frequency sweep method is rather insensitive to these problems in the frequency range of interest while the system identification approach discussed in the next section may require more careful post-processing of the data.

3.1.1 Case study: 1 MVA IBR

To illustrate identifying the bode magnitude plot directly from a frequency sweep an EMT simulation of the system shown in Figure 8 with parameters given in Table 2 has been used. This simulation has been used to implement the frequency sweep method described in the previous section.

Table 2. System Parameters.

Grid-forming units	1
Unit base power	1 MVA
Unit base voltage	480 V
Filter parameters [L,C,R]	0.1 p.u., 0.05 p.u., 0.01 p.u.
Base frequency	60 Hz
Transformer voltages	480 V to 4.16 kV
Transformer configuration	Delta-WyeGND
Transformer [L,R]	0.16 p.u., 0.004 p.u.
4.16 kV line parameters [L,R,C]	0.0017 H/km, 0.21 Ω/km, 1e−8 F/km
4.16 kV line length	1 km

The simulation contains:

1. A standard grid-following droop implementation using a SRF-PLL and current loop
2. Grid-forming control with standard proportional droop control
3. Grid-forming droop control with CERTS power limiting
4. Grid-forming control with proportional-integral droop

Moreover, for all grid-forming controls, one can select between a (i) single-loop setup in which the reference voltage phase angle and magnitude from the outer grid-forming control is directly provided to the inverter modulation scheme, and (ii) a dual-loop setup with cascaded inner current and voltage control that is used to track the voltage phase angle and magnitude reference from the outer grid-forming control at the converter AC terminal.

The resulting Bode magnitude plot for frequency and active power are shown in Figure 9. It can be seen that the Bode plots obtained from the frequency sweep agree with the analytical predictions at low frequencies but start to deviate from the reduced-order models at higher frequencies. This observation can be explained by the fact that the simulation uses far more detailed models both of the network circuit (e.g., line and transformer) and IBR (i.e., LCL filter, discrete-time controls).

Nonetheless, the results show that the two GFM controls again satisfy the performance requirement as predicted by the analytical models in Section 2.2 up to a frequency of about 40 Hz. At this point the impact of the additional circuit dynamics and more detailed control implementation with limited sampling rate becomes apparent and limits the performance of the GFM IBRs with respect to their ability to attenuate infinite bus frequency perturbations at the IBR bus. Moreover, the detailed implementation of GFL droop control not only does not satisfy

the requirement of frequency smoothing but amplifies high-frequency perturbations and therefore does not meet the performance requirements outlined in Chapter 2.

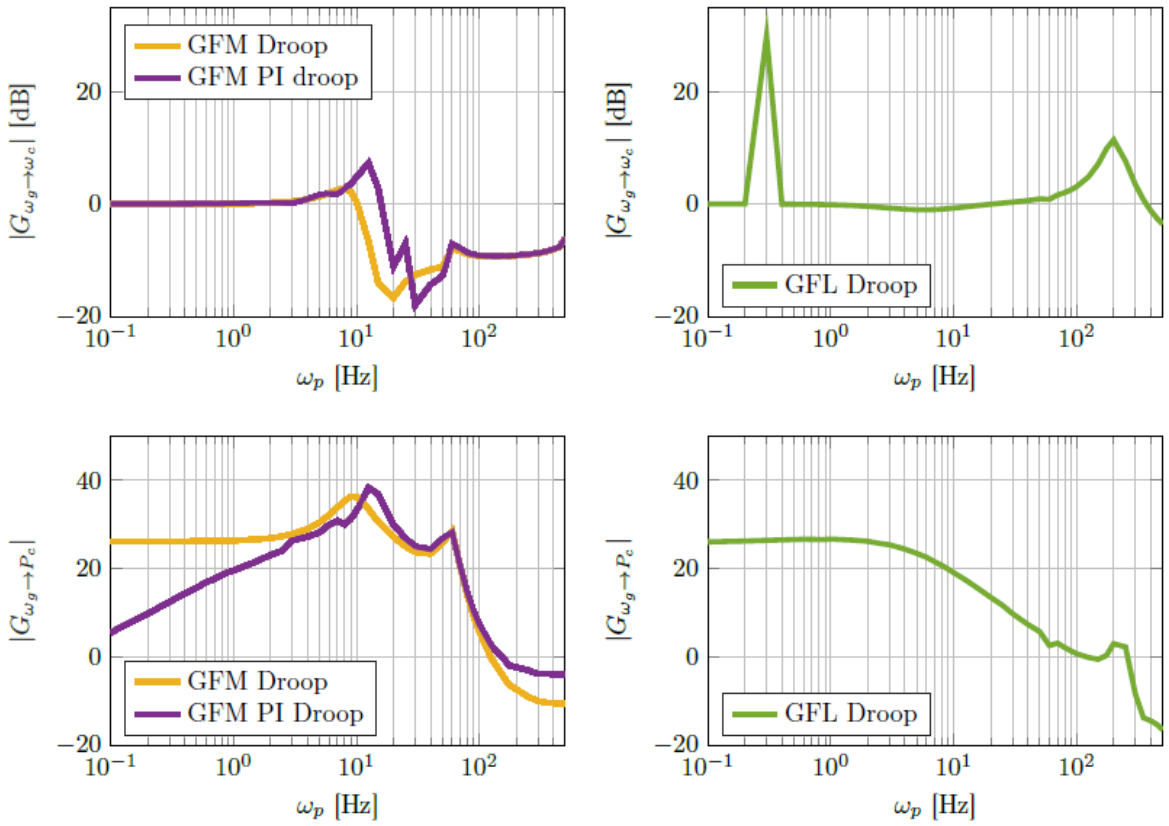

Figure 9. Bode magnitude plots for single-loop GFM droop control, single-loop GFM PI droop, and GFL droop.

Finally, we note that the response of GFM PI droop and GFM droop with power limiter coincide when the power limiter of GFM droop is active. This highlights that the small signal response of GFM droop with power limiter can be accurately modeled around two standard operating points (e.g., with and without active limiter). In particular, Figure 9 correctly shows that the IBR no longer provides steady-state droop on the average frequency once it becomes power limited but continuous to ensure a passive response with frequency smoothing in line with the GFM core functionalities defined in deliverable A3.1.1.1.

The proposed approach can also be used to discern the differences of single-loop and dual-loop GFM controls from a system-level perspective. To this end, the numerical experiments have been repeated for GFM controls with cascaded inner control loops (dual-loop) and without inner loops (single-loop) and a different set of control and network parameters. The results are shown in Figure 10. It can be seen that the results of GFM droop control without inner loops match the analytical results up to a resonance of the circuit dynamics (at 50Hz and 800Hz) that have not been considered in the simplified models used to obtain the analytical results in Section 2.2. In

contrast, the GFM with inner control loops suppresses the LCL filter resonance but is subject to a resonance at 30Hz that is attributed to a resonance of the PI controls that can be removed by re-tuning the inner controls. Similarly, the GFL control is approximately in line with the analytical results but is subject to resonance and poor damping at higher frequencies, most likely caused by interactions of the PLL dynamics with the circuit dynamics.

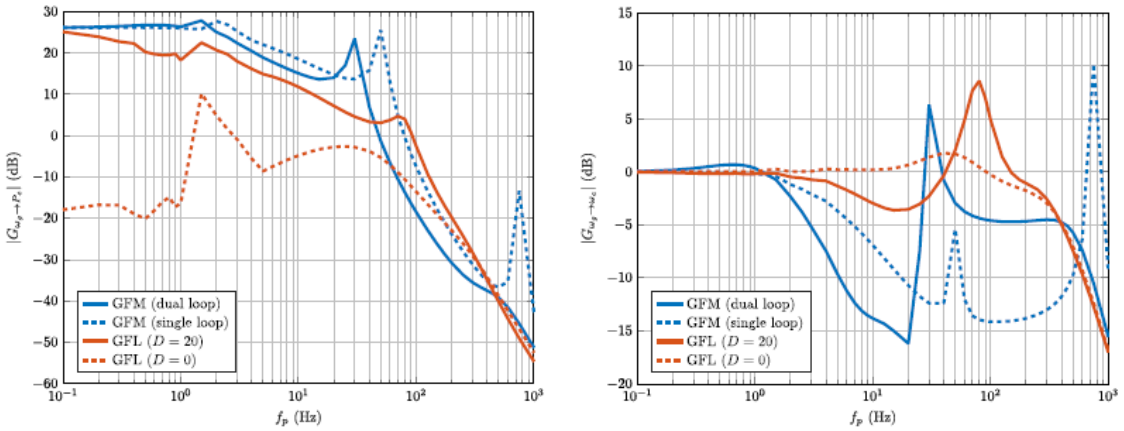

Figure 10. Bode magnitude plots for single-loop GFM droop control, single-loop GFM PI droop, and GFL with and without frequency droop.

3.1.2 Case study: Comparison of GFM controls

In a parallel effort EPRI has used the frequency sweep method to compare various GFM controls with a baseline GFL control and validate that the performance requirements formulated on the Bode magnitude plot are meaningful and not overly restrictive.

For a preliminary analysis, an average model of an inverter model is used. Perturbations are applied to the inverter terminals to the quantities of infinite bus voltage magnitude/phase angle in polar coordinates, and infinite bus voltage in rectangular coordinates. The inverter model that is used implements the full dual-loop control structure. Four types of GFM control have been included along with the cascaded voltage and current control loops. The intention of this task is to identify similarities and differences (if any) between the frequency domain characteristics of the various grid forming control structures. Each inverter resource also has a step-up transformer at its terminal. The input/output characteristics are evaluated on the high voltage winding of the inverter. The frequency domain characteristics for the following six different types of control have been evaluated:

1. Pure grid following inverter - the inverter operates on stiff P and Q control
2. Grid following with only frequency droop - the inverter provides frequency droop response but also operates on stiff Q control
3. Four different types of grid forming control have been evaluated with two types of droop control, one virtual synchronous machine control, and one virtual oscillator control

The first set of frequency domain comparisons, as shown in Figure 11, are carried out by obtaining the transfer function between (i) inverter reactive power (Q) as the output and infinite bus voltage magnitude ($|V_{\text{inf}}|$) as the input, and (ii) inverter active power (P) as the output and infinite bus voltage angle (θ_{inf}) as the input. It can immediately be seen that the characteristics of the grid following inverter technology with stiff P and Q injection stands out from the rest of the characteristics. Once the grid following resource starts to provide frequency support, its characteristics may align with the rest of the grid forming inverters. However, this is only so because the grid following inverter is providing frequency support at the inverter level, and as a result, its response is fast. If the frequency response was provided at the plant controller level instead of the inverter level, the response characteristics would not align. But only providing frequency support does not make a grid following inverter a grid forming inverter. The presence of fast voltage support is also critical and crucial.

The difference between fast voltage control and slow voltage control at the inverter level is observable from the frequency domain characteristics shown in Figure 12. With slower voltage control, the response has a drop off at a much higher frequency.

The frequency domain transfer functions shown in the previous two figures also show the similarity in characteristics across different grid forming structures. This similarity is important to identify as it indicates that transmission planners do not need to necessarily know the type of control architecture used within the grid forming inverter as long the required characteristics are obtained.

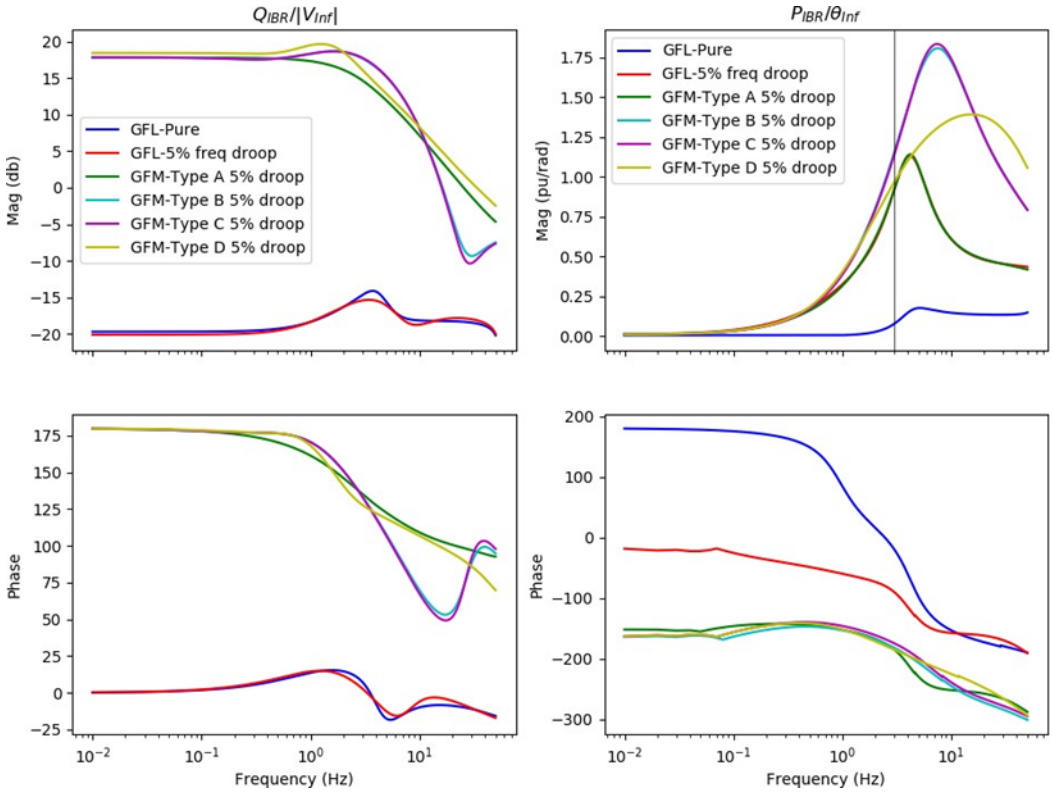

Figure 11. Comparison of frequency domain transfer functions across different types of inverter controls.

The difference in frequency domain characteristics for change in frequency droop percentage and voltage droop percentage are shown in respectively in Figure 13 and Figure 14. Here, the intent of showing these curves is to showcase the information that could be obtained from the frequency domain characteristics to complement time domain requirements and specifications.

These curves however do not address the relationship between the network frequency and the inverter frequency. Essentially for robust grid forming behavior, it would be beneficial if the inverter controls react to changes to grid frequency only when the change is in a low frequency range. If the inverter controls react to grid frequency changes over a high frequency range, then there is a chance of the inverter contributing to an instability in the network. This is because since inverter controls usually have a small time constant, their reaction to higher frequency changes can give rise to mismatches between their injection into the network and the needs of the network.

The frequency domain characteristics of the various inverter control types are shown in Figure 15. Here, the transfer function that is used is the inverter terminal voltage angle (θ_{IBR}) as the output and the infinite bus angle (θ_{inf}) as the input. Since both input and output quantities denote phase angle, the transfer function can be used as a proxy for a frequency transfer function. The curves show that a pure grid following inverter would

not attenuate the higher frequency disturbance and would instead react to it. However, as frequency support and grid forming properties are added to the inverter control, the control starts to attenuate higher frequency disturbances thereby improving the stability margin of the network.

Moreover, GFM Type A does not provide the same level of high-frequency disturbance attenuation as GFM Type B to GFM Type D. As is GFM Type A does not have the high-frequency roll off characteristic specified in Section 2.1.3 and instead shows a similar response to the analytical model of a GFL IBR with frequency droop.

Now, a question arises as to the stability that can be provided by GFM-Type A. Broadly speaking, all four types of GFM control have a similar time domain response for events that result in the formation of a 100% IBR system and for subsequent faults in the network. To further evaluate the performance of the control, the performance of GFM Type A and GFM Type B are compared in a test system containing a synchronous generator, a synchronous condenser, a load model consisting of different types of three- phase induction motors, static load, and single phase DER. Further, two GFM IBRs each of 100 MVA are used. The objective here is to bring about the formation of a 100% IBR network by tripping the synchronous condensers and tripping the synchronous generator at t = 11 s.

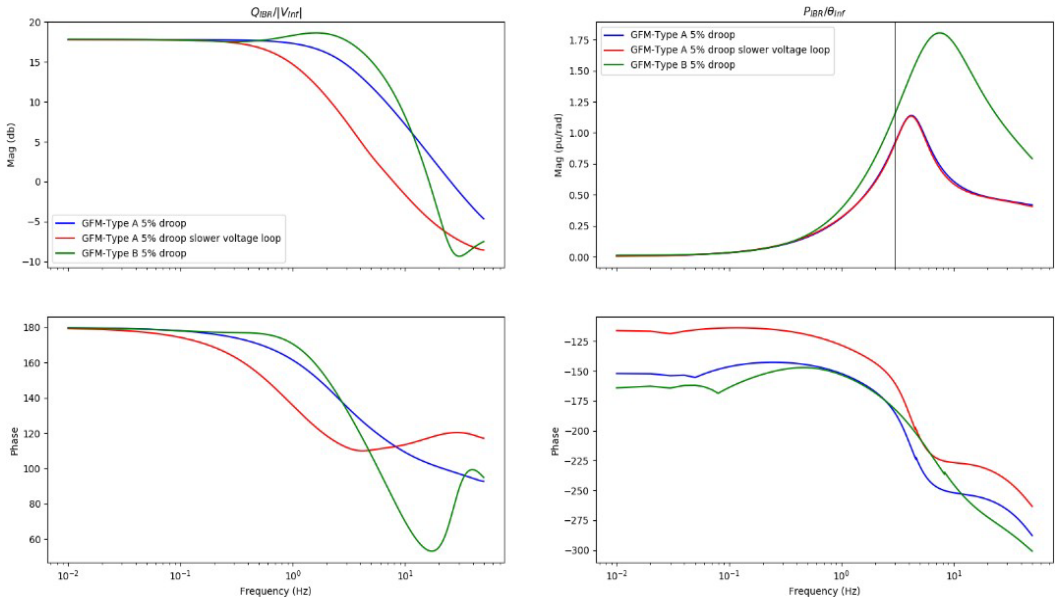

Figure 12. Comparison of frequency domain transfer function with slow voltage control on Type A grid forming inverter.

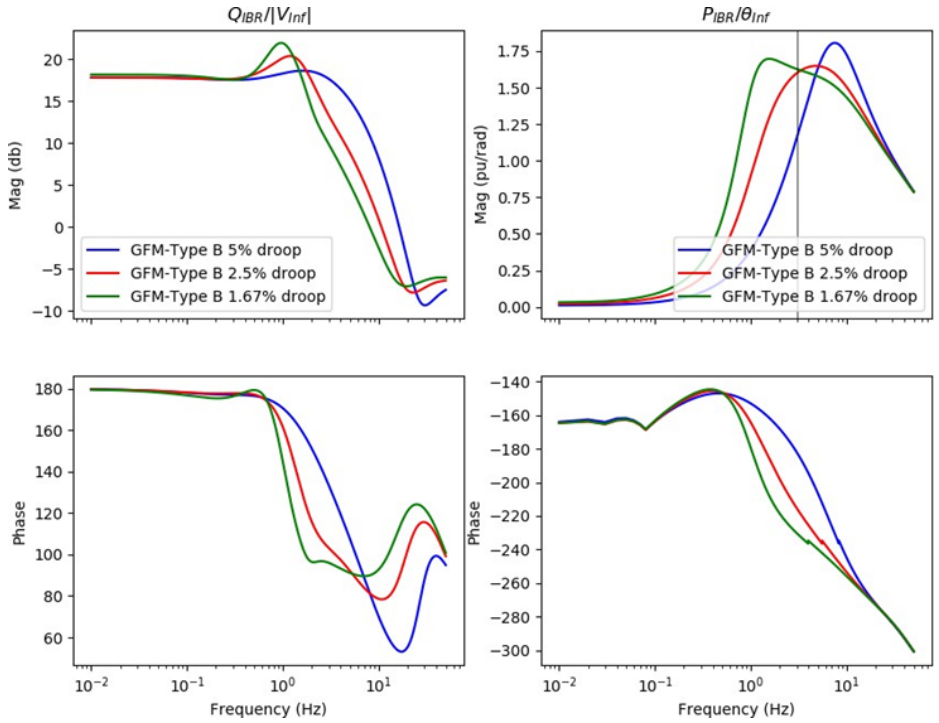

Figure 13. Comparison of frequency domain transfer function with various values of frequency droop gain, at fixed 5% voltage droop.

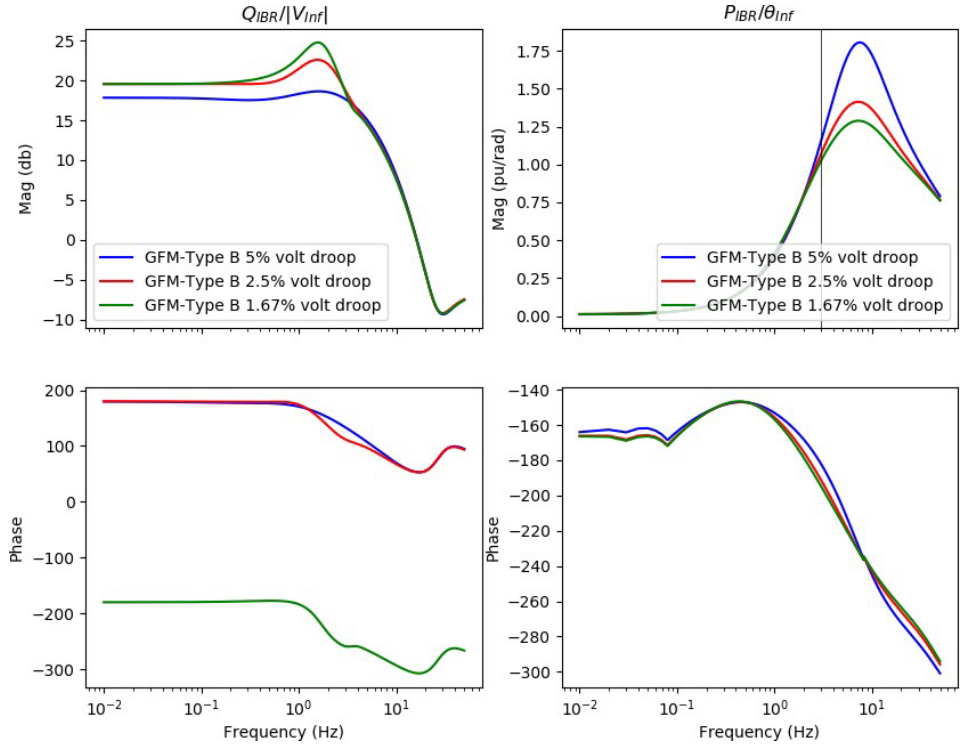

Figure 14. Comparison of frequency domain transfer function with various values of voltage droop gain, at fixed 5% frequency droop.

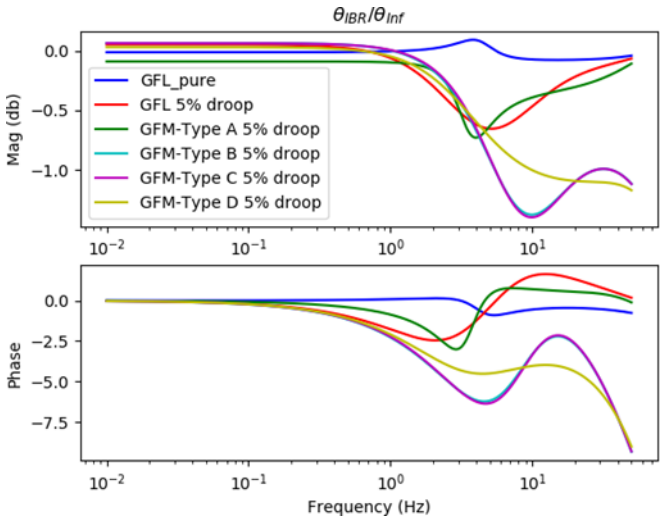

Figure 15. Comparison of frequency domain characteristics of across different inverter control types to assess ability to ride through high frequency disturbances in the network.

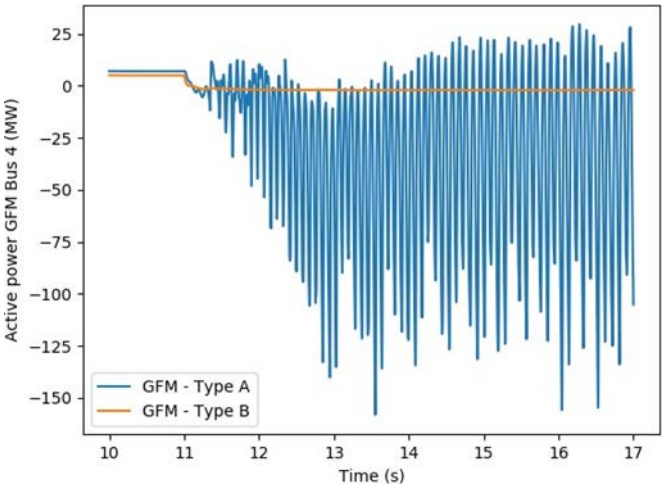

Figure 16. Comparison of GFM Type A and GFM Type B behavior for the formation of a 100% IBR network with a variety of different dynamic devices.

Both GFM devices have the same control settings and values of gains. The active power output of one GFM IBR is shown in Figure 16. It is seen that while GFM Type B is able to successfully remain stable in the system following the trip of the synchronous generator at $t = 11$ s, GFM Type A is unable to maintain stability in the network. Now suppose GFM Type A controls are re-tuned to provide an increased stability margin for high frequency disturbances, the transfer function response is obtained as shown in Figure 17. The improvement in stability margin is brought about by tuning the voltage control loop in the control structure. It should be mentioned here that this re-tuning is not necessarily the optimal settings of the control. However, the application of the concept of the transfer function and frequency domain characteristics is showcased. It can be seen from Figure 18 that now, GFM-Type A is also able to bring about stable operation of the network once a 100% IBR system is formed.

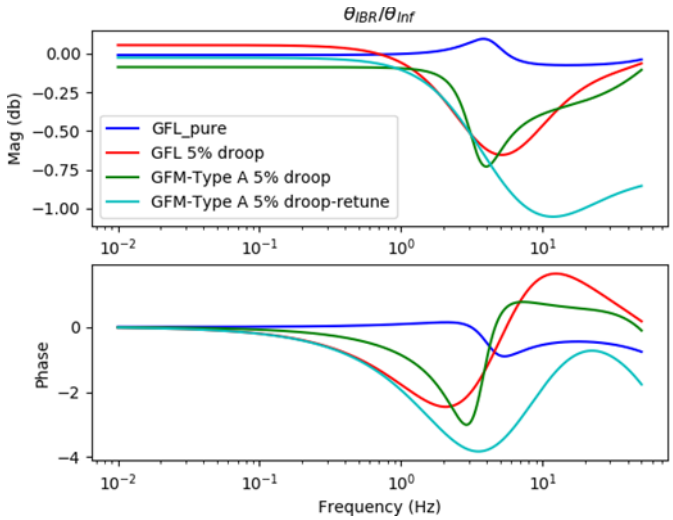

Figure 17. With re-tune of GFM Type A controls, comparison of frequency domain characteristics of across different inverter control types to assess ability to ride through high frequency disturbances in the network.

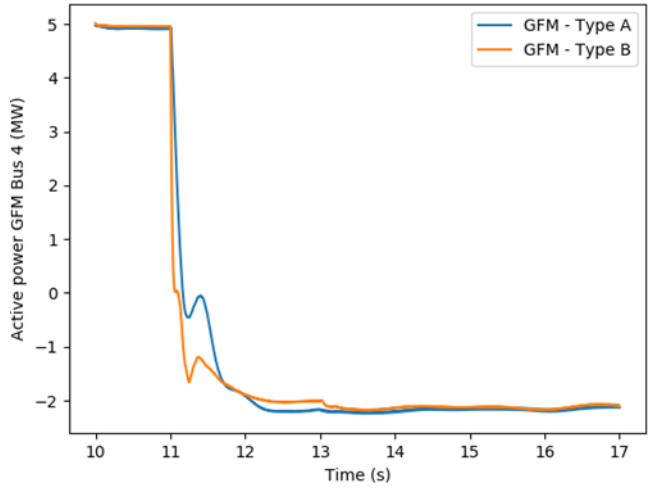

Figure 18. After re-tuning of GFM Type A control, comparison of GFM Type A and GFM Type B behavior for the formation of a 100% IBR network with a variety of different dynamic devices.

3.2 Subspace system identification

An alternative approach to the frequency sweep considered in the previous section are system identification methods that use a sequence of input and output data to directly identify a linear state space model or transfer function model that captures the input-output dynamics of the system. The most widely used method are so-called subspace identification methods. In the context of the problem at hand, the key advantage of system identification methods in general is that no frequency sweep is required but any sufficiently rich excitation signal can be used to perturb the inputs to the system and obtain a dynamic model either as a linear state space system or transfer function. Typically, this significantly reduces the amount of data that needs to be captured. Moreover, the system identification approach directly produces a model that could be

used to simulate the IBR response (i.e., in a small-signal sense), produce the Bode plots used in the previous chapter to formalize performance specifications, or to apply any other linear system analysis method. On the other hand, a key difficulty of using system identification methods is that one needs to select the order of the system to be identified in advance. This requires a priori knowledge about the system and its controls. A particular risk is so-called overfitting that occurs when a model is identified that is of higher order than the plant, faithfully represents the data used for identification, but fails to interpolate or extrapolate the system response to inputs not used for system identification.

For this work, a rough estimate of the plant order can be obtained from the reduced-order models developed in Section 1.2. Nonetheless, as the following examples show typically the system identification process needs to be repeated iteratively for models of different order until a sufficiently low dimensional model is found that represents the original system well. Thus, overall this process is more involved than the simple frequency sweep discussed in Section 3.1 but also provides output (e.g., a linear model) that can be more easily used for analysis than the graphical model (i.e., Bode or Nyquist plot) obtained from the frequency sweep method. The remainder of this section uses two cases studies to illustrate the results that can be obtained using system identification methods.

3.2.1 Case study: low-order transfer function model

To illustrate the system identification approach, we first revisit the case study used in Section 3.1.1 and consider an implementation of standard GFM droop control. Input-output data is collected for a pseudorandom binary sequence (PRBS) input signal using the same EMT simulation as in Section 3.1.1. The MATLAB system identification toolbox is used to apply a bandpass filter (0.1 Hz to 500 Hz) and subspace identification method. For brevity of the presentation, we are focusing on the transfer function from infinite bus frequency (angle) to IBR bus frequency (angle). Based on the analytical models derived in Section 1.2 using a quasi-static network model one would expect the transfer function to have at least two poles and no zeros. Using a model that captures the inductive-resistive dynamics of the line, transformer, and filter one would expect the transfer function to have at least four poles and no zeros. Additional poles and zeros arise due to, e.g., inner control loops and the LCL filter of the GFM IBR. Indeed, the transfer function model estimated for two poles and no zeros, and four poles and no zeros do not fit the time domain data or bode plot (obtained using a frequency sweep) well.

The bode plot for the transfer function identified from infinite bus voltage phase angle to IBR bus voltage phase angle (on the low voltage side of the IBR transformer) and four poles and two zeros is shown in Figure 19. It can be seen that the bode plot of the identified transfer function approximates the bode plot obtained from the frequency sweep well, except for a small peak at 60 Hz. Further increasing the model order to six poles and two zeros also allows to capture the peak at 60 Hz (see Figure 20).

While these results are encouraging, they also highlight the difficulty in selecting an appropriate model order in the system identification process. This aspect will be discussed further in the next case study that considers identification of a more detailed multi-input/multi-output model.

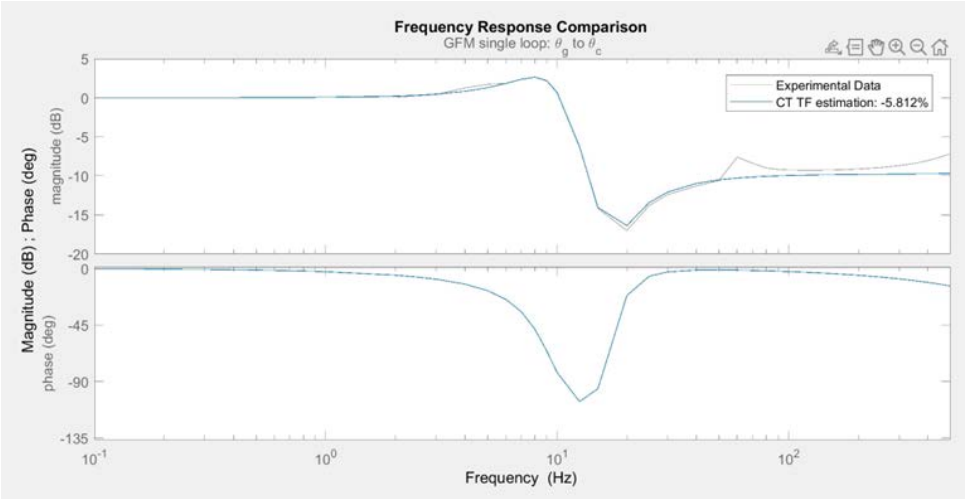

Figure 19. Bode plot from infinite bus frequency to IBR bus frequency for GFM droop control from a frequency sweep (grey) and for a transfer function model with four poles and two zeros obtained using a subspace identification method. Phase is not plotted for the frequency sweep.

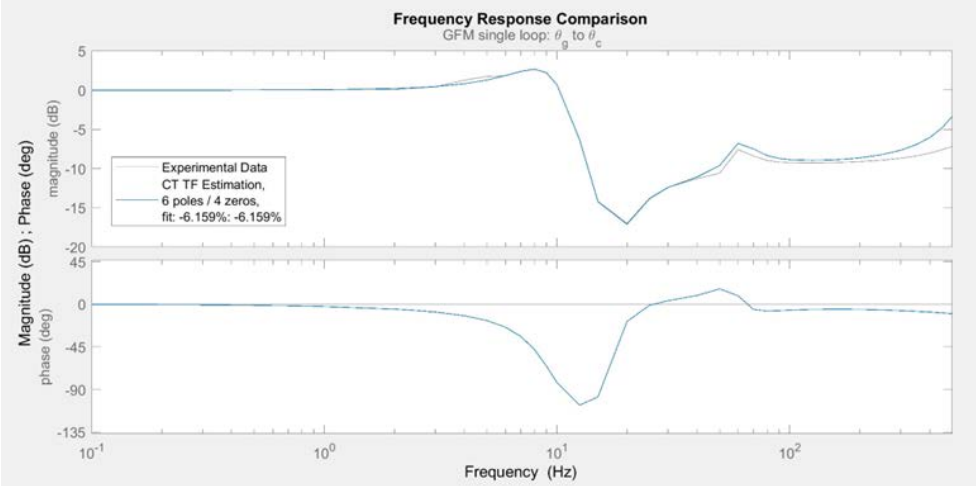

Figure 20. Bode plot from infinite bus frequency to IBR bus frequency for GFM droop control from a frequency sweep (grey) and for a transfer function model with six poles and four zeros obtained using a subspace identification method. Phase is not plotted for the frequency sweep.

3.2.2 Case study: detailed model using N4SID in MATLAB

To evaluate the performance of subspace system identification a case study using a blackbox model of an IBR plant has been conducted. The aim is to develop an input-output model of GFM inverters. It is assumed that the IBR resource has a blackbox model and the aim is to carry out a set of tests that allow for determination of grid forming capability. The first step in the creation of an input-output model will be to assess the overall shape of poles and zeros of a generic GFM IBR. For this case study, a system of a single inverter connected to an infinite bus has been prepared (see Figure 21).

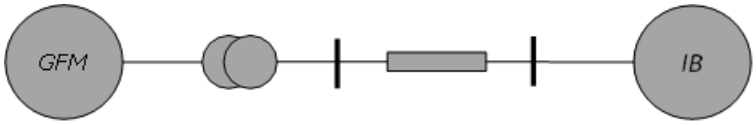

Figure 21. System model of a GFM IBR connected to an infinite bus.

The GFM IBR is represented by a PV plant with 80 inverters of 2.5 MVA rated capacity. The plant parameters are described in Table 3.

Table 3. System Parameters.

Grid-forming units	80
PV plant unit base power	2.5 MVA
Inverter Series reactance	0.1 p.u.
Transformer [L,R]	0.11 p.u., 0.001 p.u.
Line impedance [L,C,R]	0.037 p.u., 0.10 p.u., 0.003 p.u.

By linearizing the model response around a stable operating point of $P_{GFM} = 0.5$ p.u., it is possible to obtain small signal model of the system. The Pole-zero representation of such the system is shown in Figure 22.

Inspecting the lower frequency range of the pole-zero map plot allow us to observe two sets of conjugated poles (green and blue pairs in the figure) which are dominating the dynamic response. A third cluster of poles in the red circle will have faster transient with less impact on the response due to a lower real part value. Additionally, the dynamic of poles located closer to the origin are mainly canceled by the proximity of zeros and thus showing no meaningful impact in the dynamic response.

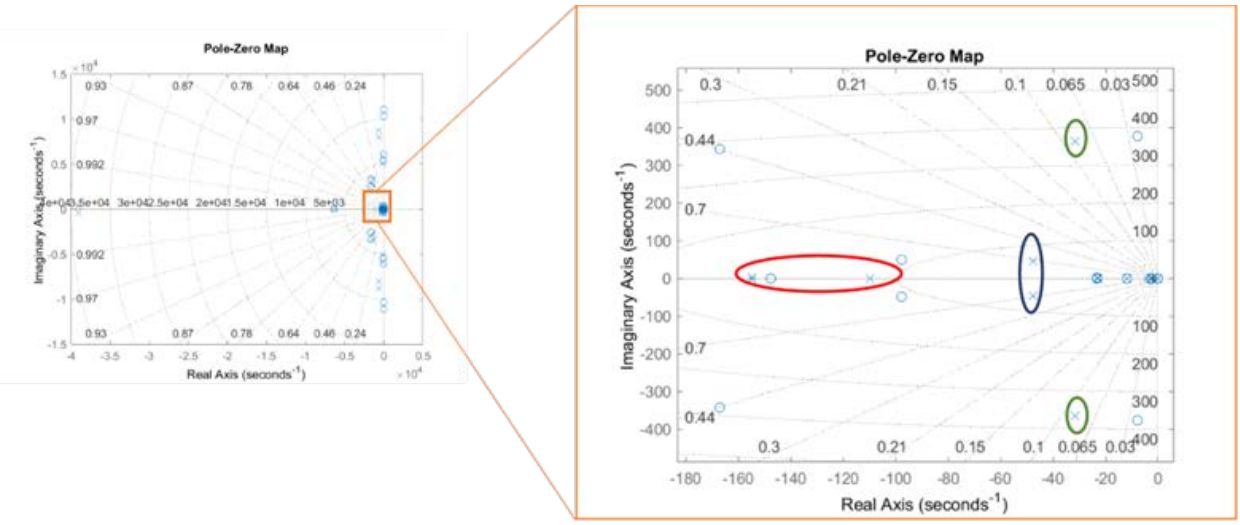

Figure 22. Pole-zero map of the reference system.

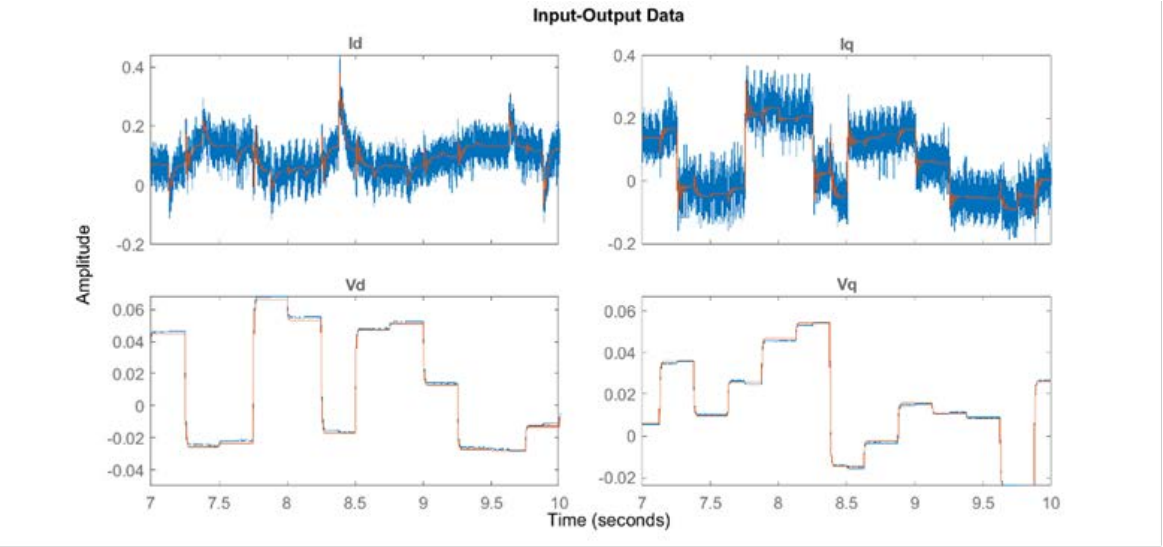

Figure 23. Input-Output response of the averaged and detailed PSCAD model of the PV plant.

In the upper frequency range of the plot, it is possible to observe two conjugated pole pairs that might play a role in the system response, however, due to its higher frequency they might be not relevant for power system studies, which is the focus of this task. The outcome of this task will concentrate on replicating the most important modes of the system driving the higher energy content of the dynamic response, focusing on those poles that are relevant for power system studies.

To reproduce fictitious data from a hypothetical black box model, a PSCAD model has been prepared using all relevant information of the GFM-IB system described previously. This model has been prepared in two different versions: 1) a detailed model of the converter, including IGBTs and DC link boost converter; 2) a simplified averaged response model of

the converter. The reason for considering these two variants is that the black box model can be derived from any of these two sources.

To produce measurement data, a response from the GFM is induced by a series of random voltages steps that are imposed by the IB at its point of connection. The result of this excitation can be observed in the following figure. From this, it can be observed that the response from both models is the same expect for the high frequency components introduced by the converter in the detailed model (blue line in Figure 23).

The first step towards the construction of an input-output model is the system identification of the model formed by the GFM and the IB. This task will allow us to construct the mathematical model that will describe with a certain degree of precision all the dynamics associated between inputs and outputs of the unknown system.

For this implementation, the algorithm numerical subspace state space system identification (N4SID) has been selected. Although the description of this algorithm will not be covered in this report, it has been selected due to its iterative approach which represents a powerful alternative to classical system identification techniques. To use N4SID, a larger algorithm has been coded which in-turn calls N4SID internally. The objective of this is to search for the best combination of two parameters: the system order and frequency threshold for a low pass filter. The resulting block diagram of the algorithm is shown in Figure 24.

The algorithm receives as input to parameter arrays which are:

- System order: array of integer values for possible system orders to be use in N4SID.
- Filter thresholds: array of real values for all frequency thresholds to be used in a 5th order butter- worth preconditioning filter.
- Additional hyperparameters: The N4SID frequency fit search area can be limited to a desired value.

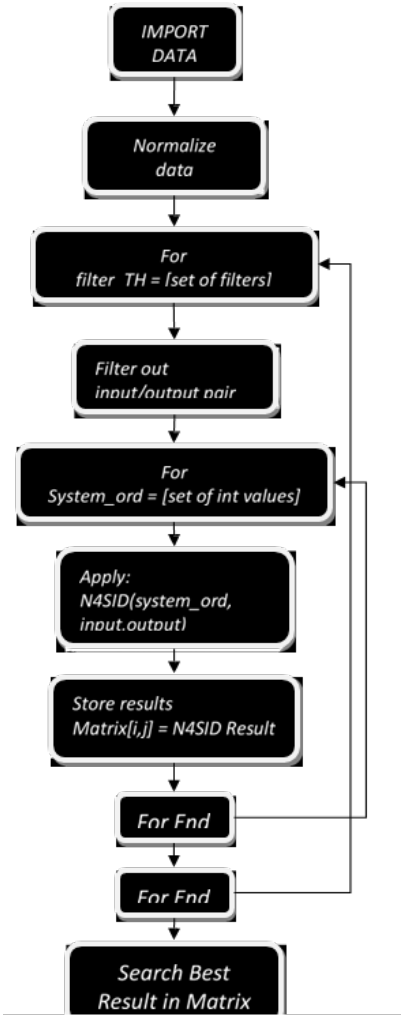

Figure 24. Overall system identification algorithm.

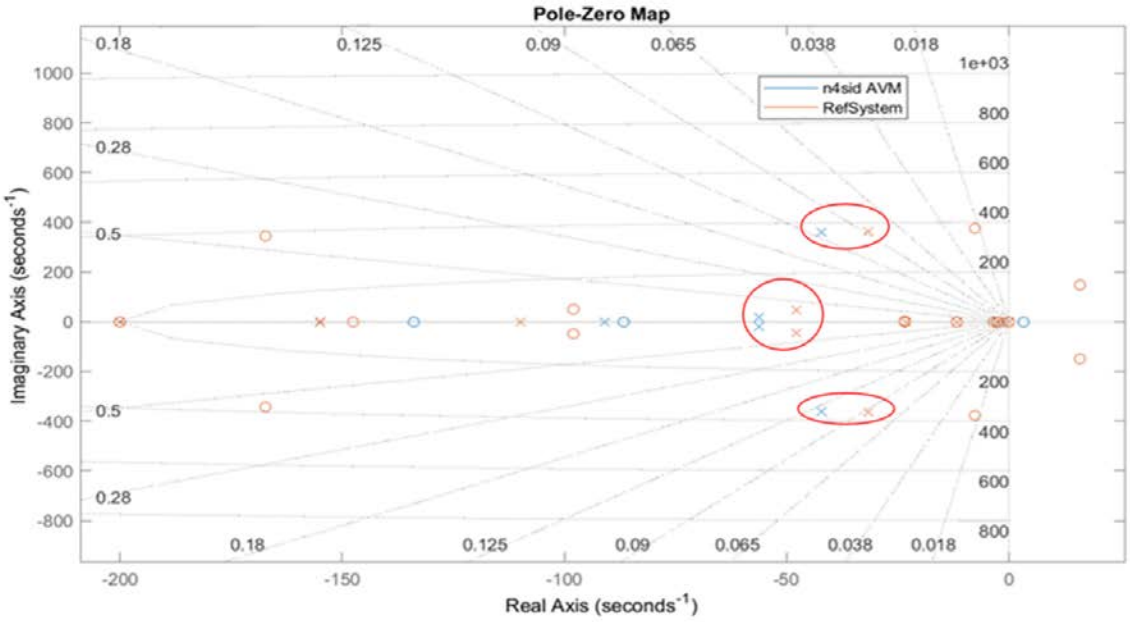

Figure 25. Pole-Zero map of the Average Model system identification. Dominant poles circled in red.

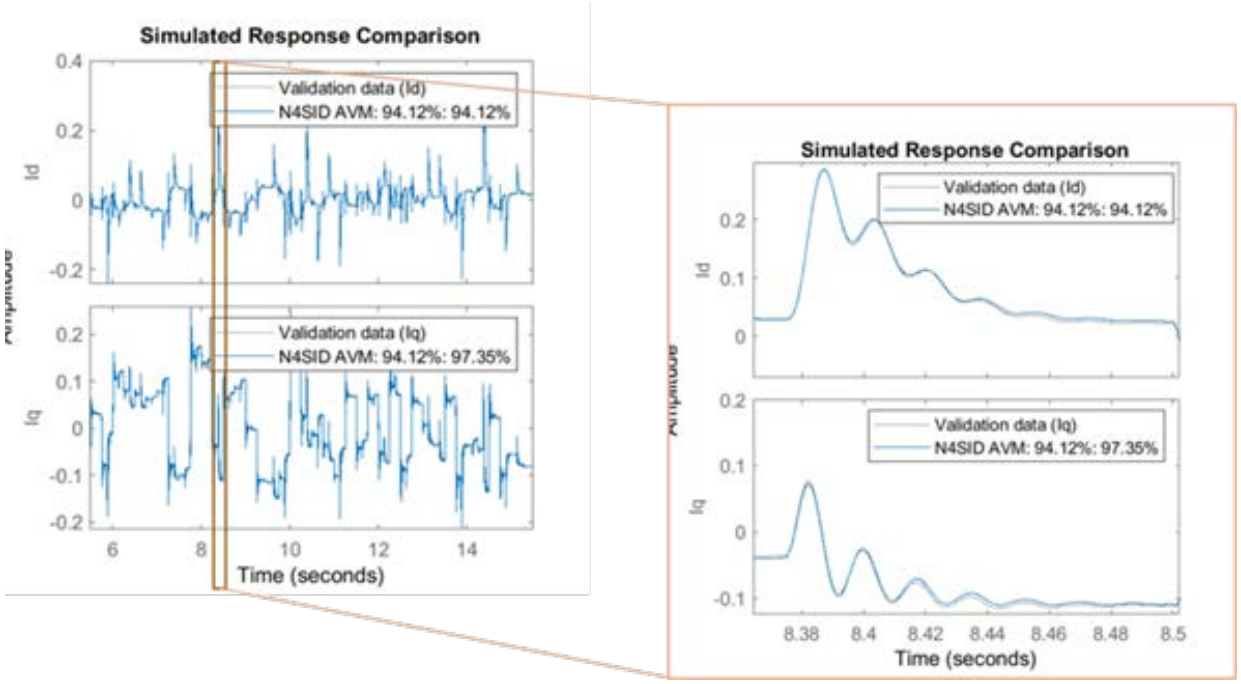

Figure 26. Simulated Response of the reference model and model obtained using N4SID.

The algorithm starts-up by normalizing the imported data. Normalization is a crucial step as the model is only valid in a very well-defined region of operation. This means that start sequence, mean values and trends need to be removed. Finally, all input-output values are scaled to be in

the range of [0, 1]. Next, a fitting Matrix is constructed by crossing all possible combinations of the previously defined parameters and sending them to N4SID. The outcome of the algorithm is a Matrix with all fitting percentages for all possible parameter combinations. Finally, the best result can be simply selected from this matrix. This algorithm has been applied to both models (Averaged and Detailed models) with the aim of obtaining the best possible system within the search horizon of those two parameters.

The best fitting results are shown for the averaged model. To account for identification precision, the results are later compared against the linearized small signal model obtained previously. Figure 25 shows that, despite having a slightly higher damping, the dominant poles have been correctly identified. Despite this, the time domain simulation of the input-output model obtained shows a good fit (Figure 26).

The system identification algorithm applied to the detailed model produced the following Matrix of fit percentages (see Figure 27). In this case, the combination of system order eight and preconditioning filter with threshold of 339.4105 rad/s results in the best fit.

Similarly, as with the previous result, the poles identified are more damped than the reference system prediction (see Figure 28). However, examining the time domain simulation, it can be seen that the model response closely approximates the mean value of current output (see Figure 29 and Figure 30). As can be seen from the results, the System Identification approach can provide an accurate representation of the dynamics of the system for both the averaged and detailed models. However, the algorithm's output is highly dependent on the parameter boundaries that were chosen for the algorithm. When the boundaries are too broad, the system tends to become overfitted and exhibit undesirable behaviors by concentrating on faster transients while ignoring crucial information in the lower frequency spectrum.

A number of techniques can be used to isolate the GFM transfer function from the identified closed GFM IB system. This approach will be pursued in future work to close the loop on the results in the previous chapters of this report. Future work will focus on efforts to overcome these limitations by, e.g., using a moving average with various preconditioning filters, use of optimization techniques to implement a search algorithm that is more reliable than the algorithm shown in Figure 24. The goal of these improvements is to deliver a result that is more reliable and no longer dependent on the initial search boundaries of parameters proposed.

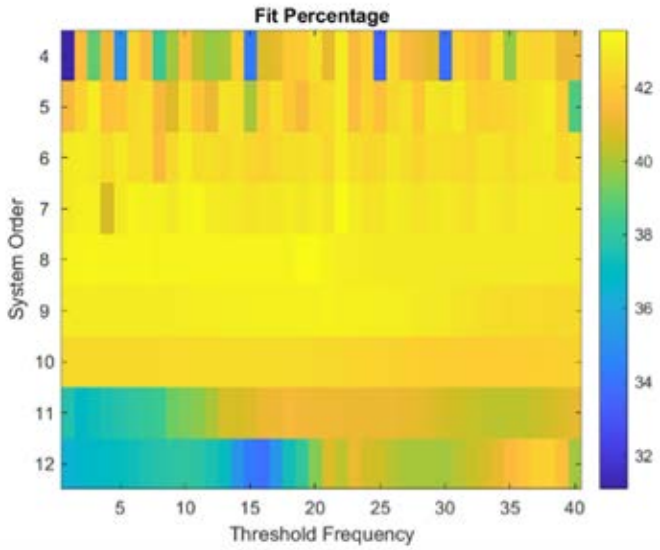

Figure 27. Colored table with fit percentages.

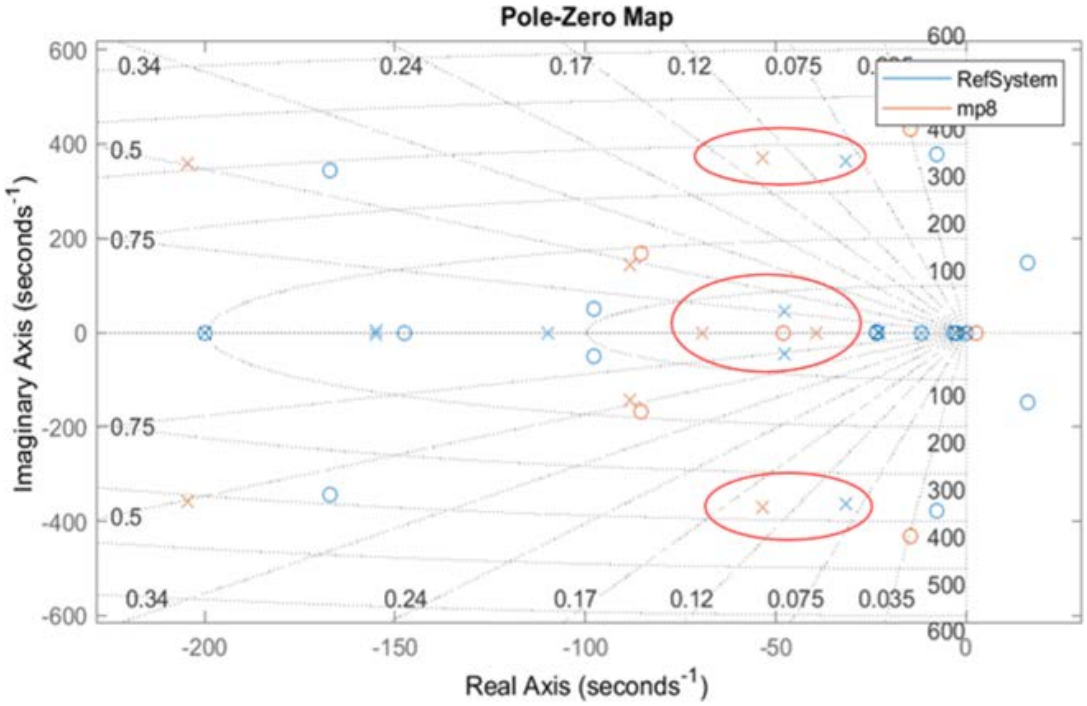

Figure 28. Pole-Zero map of the Detailed Model obtained by system identification.

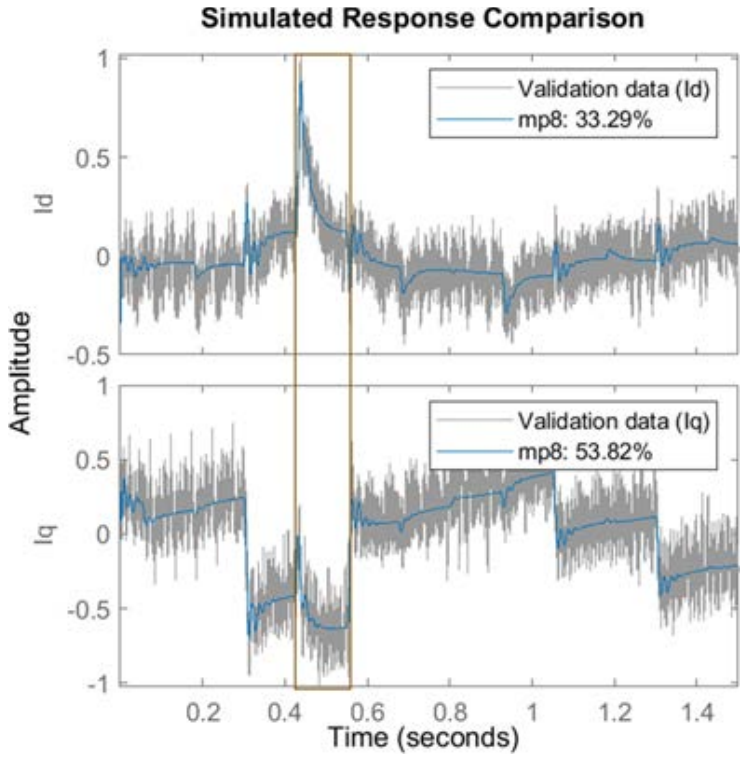

Figure 29. Simulated Response of the reference model and identified model.

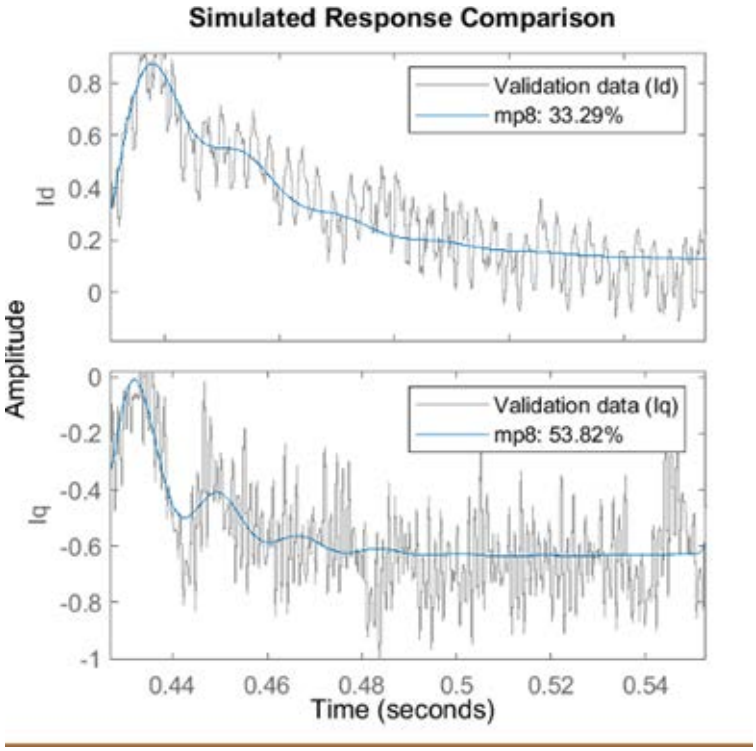

Figure 30. Detailed view of the simulated Response of the reference model and identified model.

References

[1] B. Kroposki et al., “UNIFI specifications for grid-forming inverter-based resources - version 1,” UNIFI Consortium, Tech. Rep. UNIFI-2022-2-1, 2022.

[2] D. Groß, “Compensating network dynamics in grid-forming control,” in Allerton Conference on Communication, Control, and Computing, 2022.

[3] M. Chandorkar, D. Divan, and R. Adapa, “Control of parallel connected inverters in standalone ac supply systems,” *IEEE Trans. Ind. Appl*., vol. 29, no. 1, pp. 136–143, 1993.

[4] J. Rocabert, A. Luna, F. Blaabjerg, and P. Rodríguez, “Control of power converters in ac microgrids,” *IEEE Trans. Power Electron*., vol. 27, no. 11, pp. 4734–4749, 2012.

[5] S. D’Arco, J. A. Suul, and O. B. Fosso, “A virtual synchronous machine implementation for distributed control of power converters in smartgrids,” *Electr. Pow. Sys. Res*., vol. 122, pp. 180–197, 2015.

[6] J. Schiffer, D. Goldin, J. Raisch, and T. Sezi, “Synchronization of droop-controlled microgrids with distributed rotational and electronic generation,” in IEEE Conf. on Dec. and Contr., 2013, pp. 2334–2339.

[7] G.-S. Seo, M. Colombino, I. Subotı`c, B. Johnson, D. Groß, and F. Dörfler, “Dispatchable virtual oscillator control for decentralized inverter-dominated power systems: Analysis and experiments,” in IEEE Applied Power Electron. Conf. and Exposition, 2019, pp. 561–566.

[8] F. Dörfler and D. Groß, “Control of low-inertia power systems,” *Annual Review of Control, Robotics, and Autonomous Systems*, vol. 6, no. 1, 2023.

[9] R. H. Lasseter, Z. Chen, and D. Pattabiraman, “Grid-forming inverters: A critical asset for the power grid,” *IEEE Trans. Emerg. Sel. Topics Power Electron*., vol. 8, no. 2, pp. 925–935, 2020.

For more information, visit:

www.energy.gov/eere/solar/unifi-consortium